Computers in Biology and Medicine 107 (2019) 206–217

Contents lists available at ScienceDirect

Computers in Biology and Medicine

journal homepage: www.elsevier.com/locate/compbiomed

An idealized geometry that mimics average nasal spray deposition in adults: A computational study

Milad Kiaee[a], Herbert Wachtel[b], Michelle L. Noga[c], Andrew R. Martin[a], Warren H. Finlay[a,*]

[a] Department of Mechanical Engineering, University of Alberta, Edmonton, Canada
[b] Boehringer, Ingelheim, Germany
[c] Department of Radiology and Diagnostic Imaging, University of Alberta, Edmonton, Canada

ARTICLE INFO

Keywords:
Nose
Idealized
Droplets
Nares
Vestibule
Olfactory
Turbinates
Nasal
Spray
Penetration
Lungs

ABSTRACT

This work describes the development of an idealized geometry that mimics average regional deposition of nasal sprays within realistic adult nasal geometries. Previous simulation results in seven realistic nasal airways (Kiaee et al. Int. J. Num. Methods Biomed. Eng. 34: e2968, 2018) were used to establish target values of regional deposition. Characteristic geometric features observed to be common to all the realistic nasal airway geometries studied were extracted and included in the idealized geometry. Additional geometric features and size scaling were explored, in order to enhance deposition in specific regions based on the results of simulations done in preliminary versions of the idealized geometry. In total, more than one hundred thousand simulation cases were conducted across a range of particle parameters and geometric shapes in order to reach the final idealized geometry presented herein. For droplet velocities of 0–20 m/s, droplet sizes of 5–40 μm and at an inhalation flow rate of 15 l/min, regional deposition in the final idealized geometry compares favourably with average deposition in each of the vestibule, valve, olfactory, turbinate, nasopharynx, and outlet regions in the realistic geometries. The proposed idealized nasal geometry has potential for use in the development and testing of nasal drug delivery systems, allowing researchers to estimate in vivo regional nasal deposition patterns using a simple benchtop test apparatus.

1. Introduction

Nasal drug delivery is widely used for the topical treatment of rhinitis, nasal polyposis and sinusitis, as well as for non-invasive systemic drug administration via absorption through the nasal mucosa. Particle deposition within the nasal airways is an important consideration in the design and evaluation of intranasal drug delivery systems. In particular, the regional deposition pattern of drugs administered intranasally is expected to impact their therapeutic effectiveness. Many aspects of regional deposition are thought to play a role. For instance, droplets collected in the anterior nasal passages may pool and drip from the nostrils [1]. Conversely, droplets passing through the nasal cavity to the throat miss their site of action, and might penetrate to the lungs, where adverse side-effects could occur [2–4]. Although the adult nasal airway geometry exhibits complex morphology and intersubject variability [5,6], numerous in vivo and in vitro experimental studies have been performed in order to determine particle deposition in specific nasal airway geometries [7–14]. Several computational studies have also been performed using realistic nasal airway geometries [13,15–21].

Many factors can influence regional deposition of nasal sprays. These include, but are not limited to, the distributions of size and velocity of droplets emitted from nasal spray pumps, the spray cone angle, the orientation angle of the spray with respect to the nasal inlet, and the insertion depth of the spray tip into the nostril. Including variations in the numerous geometric features of the nasal airway that can also influence regional deposition patterns, the scope of numerical or experimental studies of regional deposition can become very large. For this reason, a reference idealized geometry would be extremely beneficial in reducing the computational or experimental burden, provided that measurements made using that idealized geometry could, with confidence, be expected to anticipate average values in a larger set of realistic nasal airway geometries. Furthermore, the simplicity of such a geometry would make these analyses more feasible. In experiments, fewer small-scale complex features or extreme convolutions in a given region could make assay and cleaning easier for an idealized geometry than for a realistic geometry. In simulations, an idealized geometry makes the discretization less complicated and hence the simulation is less computationally demanding.

* Corresponding author. University of Alberta, Department of Mechanical Engineering, 10-203 Donadeo Innovation Centre for Engineering, 9211 116th Street NW, Edmonton, Alberta, T6G 1H9, Canada.
E-mail address: warren.finlay@ualberta.ca (W.H. Finlay).

https://doi.org/10.1016/j.compbiomed.2019.02.013
Received 29 November 2018; Received in revised form 5 February 2019; Accepted 18 February 2019

For aerosol drug delivery to the lungs, various researchers have described in vitro methods using realistic or idealized airway geometries selected to mimic average deposition of in vivo studies [7,11,22–25]. Such idealized geometries can function as a reference for in vitro experiments or in silico simulations, facilitating prediction of in vivo behaviour at early stages of drug or device development, and allowing comparable results to be obtained between laboratories. For nasal drug delivery, a similar geometry mimicking in vivo regional spray deposition in an average sense has not been established. As a result, researchers and drug developers must rely on in vivo studies employing gamma scintigraphy to assess regional and total nasal deposition of radiolabeled drug products. The cost and time requirements associated with conducting in vivo studies are such that these studies are rarely conducted in the early stages of nasal drug product development, where they would provide invaluable feedback to developers. Accordingly, a clear need exists to develop an idealized nasal airway geometry through which to provide rapid feedback on anticipated regional deposition patterns. The availability of such a geometry would help to expedite development of novel nasal therapies and delivery devices, and could provide a reference geometry to improve repeatability of test data obtained in different laboratories.

A previous attempt to develop an idealized nasal airway geometry used a combination of computational fluid dynamics, cross sectional averaging and two-dimensional image processing [26]. Such an approach may be useful for particle penetration to the lung in which the total deposition shows a linear or nearly linear behaviour with changes in airway geometry. However, the regional deposition of particles or droplets within the nose is inherently a nonlinear function of the shape of the geometry, making a linear superposition inherently inaccurate. In other words, there is no evidence that an idealized geometry based on linear averaging of realistic geometries would mimic average of deposition in those geometries. Furthermore, an idealized geometry based on cross-sectional averages may produce complicated surfaces and make manufacturing more difficult.

For inhalation drug delivery to infants, which occurs through the nasal airways, an alternative approach has previously been taken to develop an idealized infant nasal geometry. This approach focused on geometric pattern extraction in an heuristic manner [11,24]. The approach resulted in a significantly simpler and smoother geometry that is also easier to manufacture. Although the qualitative approach towards feature extraction in these studies is less mathematically rigorous than that adopted by Ref. [26], it favours the important concept of nonlinearity with regard to shape structures.

The above considerations motivate development of an idealized geometry that mimics the average regional deposition in a target population of adult subjects with normal (non-pathological) nasal airways. The current study seeks a geometry that mimics the average regional nasal spray deposition observed in the realistic geometries reported in Ref. [27].

2. Methods

2.1. Idealization of airway geometries

Ten individual subjects' nasal airway geometries were obtained from sectional Computed Tomography (CT) scans (Fig. 1). These airway geometries were assessed as normal (non-pathological) at the time of scanning, and airways were confirmed to be normal by a radiologist reviewing the CT images. Segmentation and reconstruction of the cross sections produced three-dimensional surfaces, as described by Ref. [27]. The subjects ranged in age from 27 to 72 years old, included 7 males and 3 females, and the resulting scans extended from the nares to below the larynx regions. The use of medical imaging data was approved by the Health Research Ethics Board at University of Alberta. Because each nasal geometry has two independent and separate proximal airway paths (one for each nostril), the total number of proximal airway geometries available to us was effectively twenty.

The realistic geometries were all complex, containing numerous features at different scales. From the twenty geometries, fourteen were previously selected for a wide-ranging computational parameter space exploration [27]. In that study, deposition in six regions of each nasal airway geometry (the vestibule, valve, anterior turbinate, posterior turbinate, olfactory, and nasopharynx) was determined for varying particle diameter, spray cone angle, spray release direction, particle injection speed, and particle injection location. Fig. 2 displays the six anatomical regions of the nasal airway defined for one of the realistic airway geometries studied by Ref. [27]. The resultant regional deposition pattern sets a target for evaluating the suitability of the present idealized geometry. The geometry of the remaining six realistic nasal airway realizations was also helpful for the purposes of qualitative observation.

The realistic geometries were available in three dimensions as stereolithography (STL) files, and the global coordinate system was chosen as right handed and Euclidean. The + y direction was defined toward the back of the head and tangent to the inlet surface of the nostril. The + z direction was defined as upward and normal to the inlet and was called "up".

Slicing the surface geometries on the x-z plane resulted in a set of curves containing one or more components, each of which was a simply connected curve. Without loss of generality, we denoted each set as one cross section.

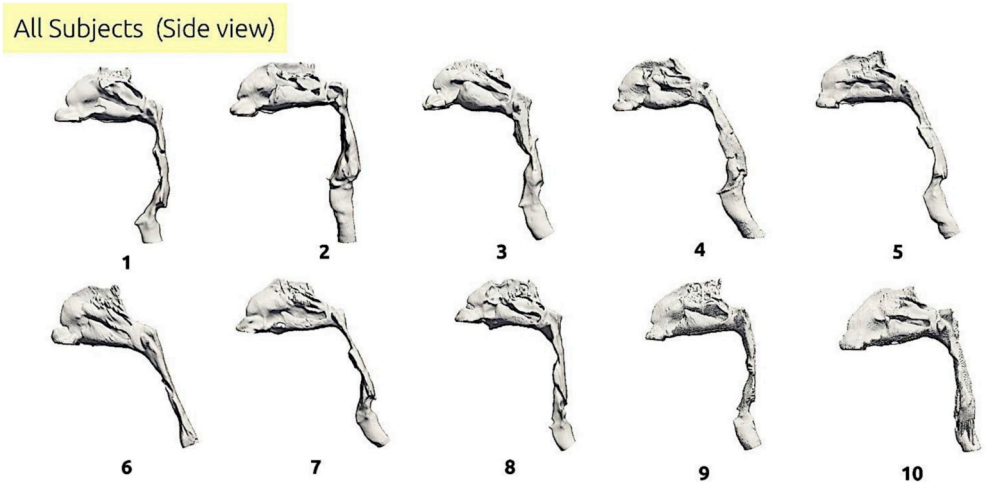

Fig. 1. Side view of the ten geometries used in this study. CFD results of seven of these geometries (subjects 1, 2, 3, 4, 6, 7 and 8) using both nostrils (one at a time) are available from Ref. [27].

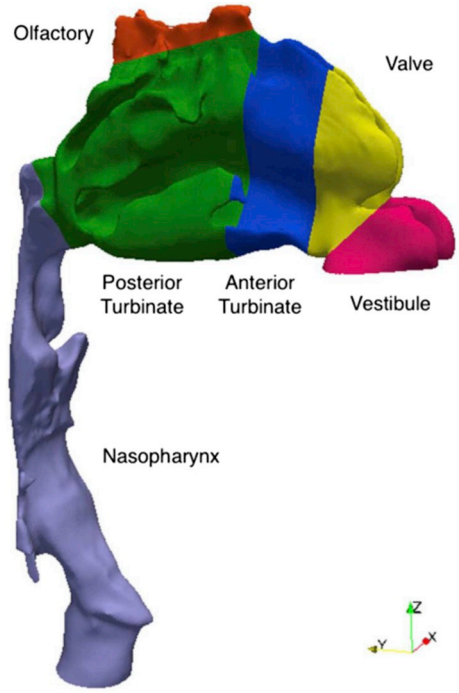

Fig. 2. The 6 anatomical regions of the nose as defined in one of the subject's geometries. Reprinted from Ref. [27] with permission.

Cross sections were seen to undergo considerable changes in shape when proceeding in the +y direction. In particular, a shape bifurcation was seen to occur within the turbinates, with the additional branch eventually turning back to the upper turbinates and creating a semi-circular cross section at the junction between the posterior turbinate and the nasopharynx. This second branch contains many small features. The center of area of its cross section traces out a nearly flat line extending parallel to the y-axis. However, the bifurcation branch reduces its z extent in a nearly linear manner and fades away in the +y direction. The lower part of the cross section rolls upward within the posterior turbinate and becomes further convoluted. The resulting Y-shape cross section vanishes as the nasopharynx is approached. Fig. 3 shows this so-called Y-shape concha. Fig. 4 shows the development of cross sections in the +y direction.

The entrance region is defined as the appended inlet, vestibule and valve regions. The shape of the entrance region is important, both because it presents an obstruction that yields deposition of high momentum particles and because of this region's role in guiding the flow (and lower momentum particles) toward the turbinate region. The shape and area of the inlet of the idealized geometry were chosen to reflect those of the realistic geometries. The entrance regions share similar characteristics across the realistic geometries, with some of these features having a direct effect on particle deposition. As an example, some of the important features of the entrance region are highlighted in Fig. 5.

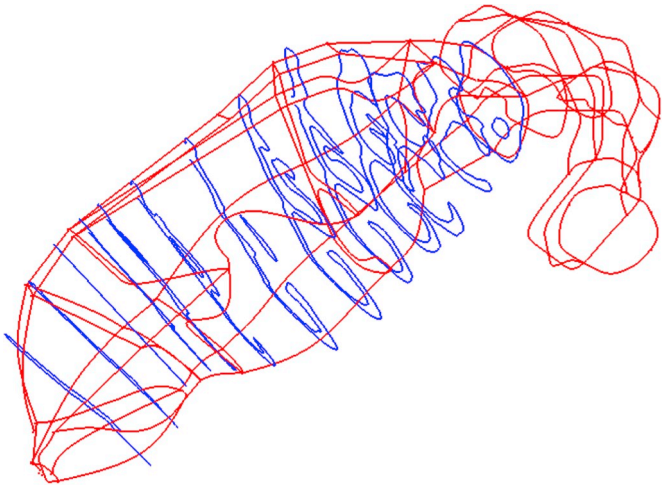

Fig. 4. Blue curves show cross sections of subject 4 as an example. The red wireframe shows an idealized sketch drawn in OpenFOAM's BlockMesh. The idealized curve considers all subjects' common features.

The air flow through the nasal airway enters from the nostril and passes the vestibule region, afterward being directed toward the turbinate region through the valve. The level of geometric complexity rises dramatically at the turbinates. Indeed, the three-dimensional development of geometric structures in this region creates cross sectional curves in x-z planes that are not simply connected. This is in contrast to the vestibule, valve, olfactory and nasopharynx regions, where the curve created by each cross section mostly stays simply connected (i.e. a cross-section curve set has only one component). Fig. 6 shows cross-sections that highlight this behaviour in one of the realistic geometries.

The appearance of the non-simply connected curves in cross-sections within the turbinate region of the realistic geometries could be addressed in several ways in an idealized geometry. One solution would be to introduce an independent three-dimensional surface geometry within the turbinate region of an idealized geometry. This surface

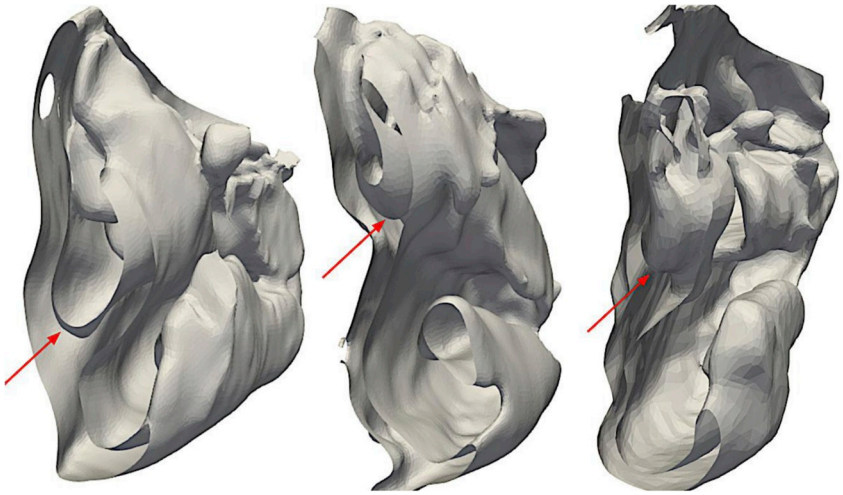

Fig. 3. Portions of the turbinate region in subjects 1, 2 and 4 are shown (left to right) around the same cut plane. A significant common feature in all geometries is the Y-shaped concha. As is pointed out by the arrow for these examples the position of this Y-shape varies in different subjects.

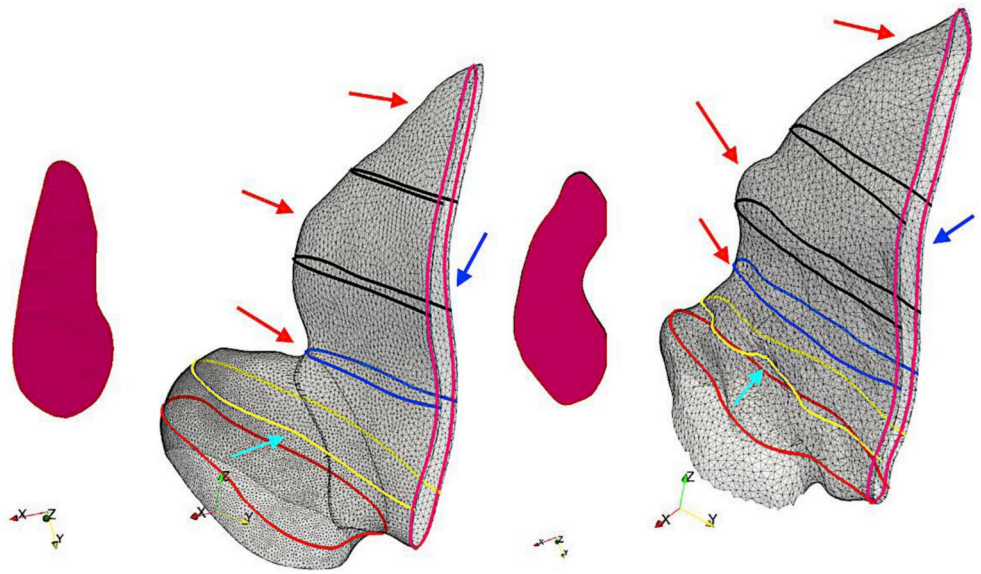

Fig. 5. The entrance regions for subject 1 and 4 are depicted. Entrance regions in all realistic geometries show similar features. Several examples of these features are pointed out by arrows here. The red arrows point to out shrinkage and expansion of the geometry when moving in the +z direction. The blue arrow shows cross section between the valve and the turbinate regions. This cross section has a vertically stretched S-curve shape. The cyan arrow shows how the cross section shrinks in the vestibule-to-valve interface from the red to the yellow cross section and expands from the yellow to the blue cross section in the +z direction. The maroon-colored section on the left of each entrance shows the inlet surface. Note the bean shape of the inlet surface.

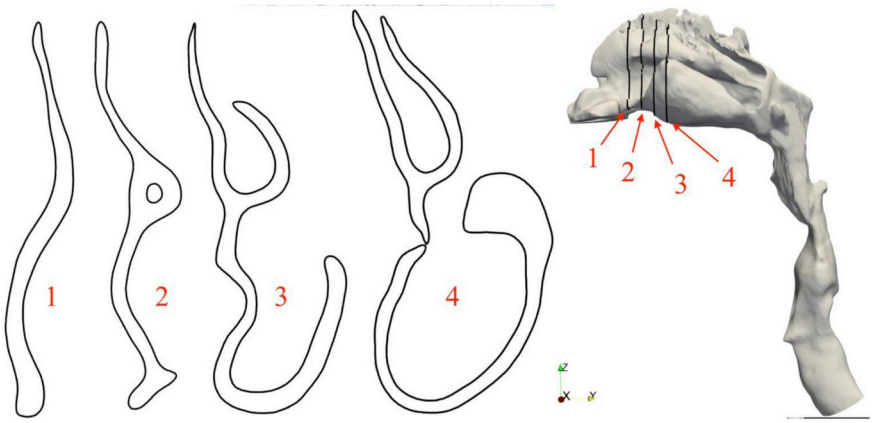

Fig. 6. Some cross sections in the realistic geometry of subject 4 are shown. Different cross sections are shown with different numbers. Note the sudden conversion of the cross section 2 where it becomes non-simply connected. The unconnected portion of the curve develops further in the + y direction as the cross-section changes.

would emulate the abrupt expansions, shrinkages and steep curves of the realistic turbinate region. Since such an object plays the role of a major obstruction in front of the flow coming from the valve, we refer to it as an obstacle. Fig. 7 demonstrates the concept of such an obstacle.

The turbinate region in the realistic geometries shows many small-scale features that can affect deposition by way of inertial impaction. In particular, as the Stokes number decreases, the probability of the deposition due to these small-scale features also decreases, meaning that smaller particles require sharper features to mimic deposition with an idealized geometry. The smaller scale features in the turbinates of the realistic geometries are expected to trap the smaller size particles. To achieve both simplicity and abruptness, the effect of the small-scale structures in the realistic geometries could be mimicked in the idealized geometry by a set of generic small objects. Indeed, this approach was found necessary in order for the idealized geometry to match average deposition in the turbinates. To this end, as one possible approach, a set of equal-sized rods was implemented in the turbinate region of the idealized geometry. This idea is inspired by the mesh filters that are widely used to capture particles from a flow. A detailed analysis of the most efficient composition of the generic object would be rigorous and outside of scope of this study. However, in practice there is a maximum size of mesh which can be used efficiently to filter particles with certain minimum aerodynamic diameters [28]. Similarly, here the size of the rods is crucial and should be chosen small enough.

Observations from CFD results in the realistic geometries in Ref. [27] also suggest an additional mechanism for particle deposition in the turbinate region. In particular, at the anterior turbinates, the flow is separated into two branches consisting of a major and minor flow. The minor flow stays nearly straight and has a smaller cross-sectional area. The major flow turns toward the side and exhibits a larger cross section. This branching of the flow partially separates the smaller particles from larger ones, with the major flow carrying only the small particles.

This particle separation mechanism resembles that in a virtual impactor. As in the case of virtual impactors, large particles follow the straight path. By contrast, small particles diverge with the major flow. In our idealized geometry, a fraction of the small particles should be collected by the aforementioned rods to mimic the dynamics of realistic nasal airway turbinates. Additionally, the boundary between the minor and major flows is an obstacle and functions as a conventional body impactor.

2.2. Computational fluid dynamics of airflow

Fluid motion in the idealized nasal airways was simulated by solving the incompressible, laminar Navier-Stokes equations. This was accomplished by using the Open-Source Field Operation and Manipulation (OpenFOAM) version 3.0.1 (OpenFOAM Foundation Ltd, UK). OpenFOAM is a collection of libraries and applications written in C++ and covers a broad range of applications in the field of scientific

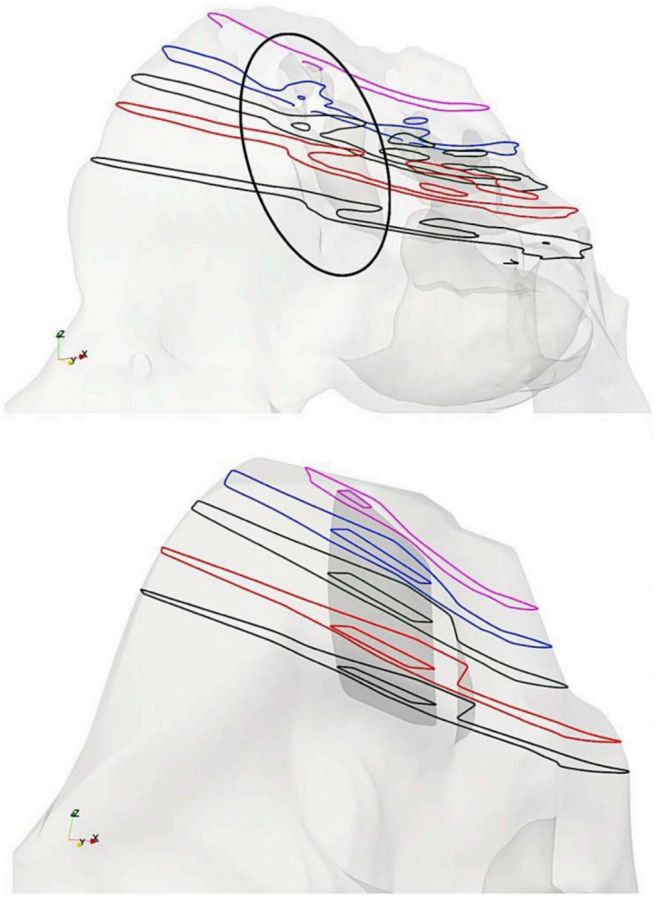

Fig. 7. The top part of the figure visualizes the geometry of subject 4 using a small amount of opacity. Cross sections in different colors are from different *xy* planes. The obstacle structure is highlighted by the drawn black ellipse. Bottom shows an implementation of the same idea in the form of an obstacle object within the turbinate region in an idealized airway geometry.

computing. Specifically, OpenFOAM solves the Navier-Stokes equations of the fluid motion using a finite volume method.

Since it has been pointed out by previous studies that the flow regimen of the adult nasal airway typically remains mainly laminar for common inhalation flow rates [8,29,30], we have assumed laminar flow in our simulations.

OpenFOAM's BlockMesh tool was applied to automate the block generation. This was performed by creating a set of control points and edges as shown in Fig. 8. Each block contains eight patches. A patch is defined by four boundary curves which are created by skeleton splines. A spline is created by defining start and end points. Moreover, a spline can be adjusted by the addition of control points that create a curved edge between the start and end points.

The surface geometry of the main wall was defined as a function of chosen patches of all blocks. Analogously, the obstacle surface was constructed within the turbinate region. For simplicity, the corners of the obstacle were chosen to define a box. Additionally, splines were defined as edges of the box. Furthermore, constraints were defined to ensure the consistency of the box topology. This measure was necessary to ensure a functional iterative process within which the shape of the obstacle was modified.

Alongside BlockMesh, most geometric manipulations were carried out using Visualization Toolkit (VTK) version 8.1.1 (Kitware Inc, USA). VTK is an open-source library for computational geometry, visualization and graphical methods. It supports various efficient and state of the art algorithms for handling several types of data structures. Moreover, VTK supports techniques for manipulation of STL files.

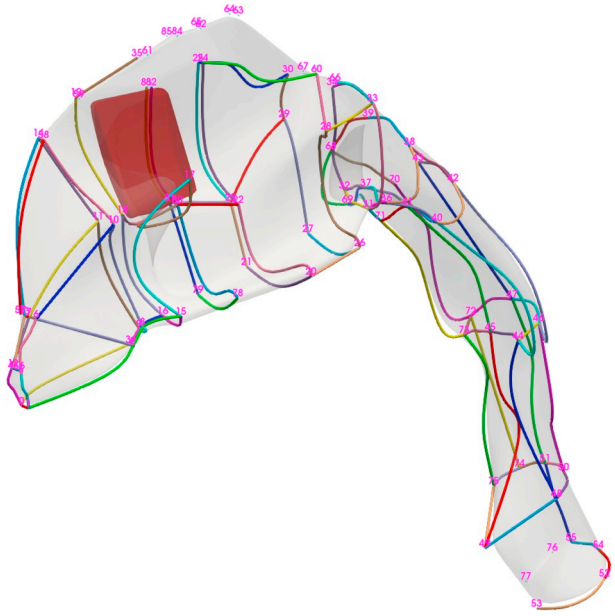

Fig. 8. The idealized geometry was created via the OpenFOAM BlockMesh tool. The red block in the middle is the obstacle and was created by using the same tool. Start and endpoints of splines are shown by numbers. Splines are curved edges connecting the points.

Since both the main wall and obstacle geometries are created parametrically, they can overlap within the iterative process. Additional constraints were defined to avoid extreme cases. However, within these limits, there are numerous combinations that result in extremely sharp angles. Even a slight overlap can produce intersection edges that result in poor quality of the CFD mesh. Various in-house codes were developed in VTK to resolve this problem in an input-output (IO) approach. These codes included methods for smoothing, clipping, closing holes with distance, closing with cap, subdivision, decimation and triangulation.

VTK was also instrumental in generating the rods, which are meant to collect only the smaller particles. Rods are inserted from the +x side of the airway and are clipped by the nearest plane of the obstacle box. This procedure was also implemented in VTK. In a trial and error approach, four rows of rods were created, each containing rods with the same y and angle γ with which they intersect the obstacle. Rods in different rows have different γ and y. Modifiable parameters for rods are the diameter of each rod d_r, the start point of the rods grid (y_s, z_s), the number of rods n_y and n_z and the distance between the center lines of the rods δ_y and δ_z in each direction.

The STL surfaces from BlockMesh underwent further repair and smoothing before being imported into OpenFOAM's SnappyHexMesh meshing tool. SnappyHexMesh offers several methods to control the refinement level in specific regions. By default, refinement regions are explicitly defined for surfaces. Moreover, extra regions are added according to the calculated feature edges. Feature edges belong to a class of objects in VTK that defines special edges such as boundaries and large surface normal gradients. OpenFOAM's surfaceFeatureExtract method extracts the features of the geometry.

SnappyHexMesh implements quality checks to ensure the validity of the computational grid. These checks included, but were not limited to, cell skewness, minimum volume, volume ratio, orthogonality and twist. The result was a mesh with three to five million hexahedral cells depending on the size of the feature edges set. As the size of this set increases, further refinement was essential. Fig. 9 shows y and z clips of a sample mesh.

With the mesh prepared, the steady state flow equations were solved for velocity and pressure fields in space. The Semi-Implicit Method for Pressure-Linked equations (SIMPLE) was used for the nonlinear outer iterations. SIMPLE is known to be an efficient solver for steady state

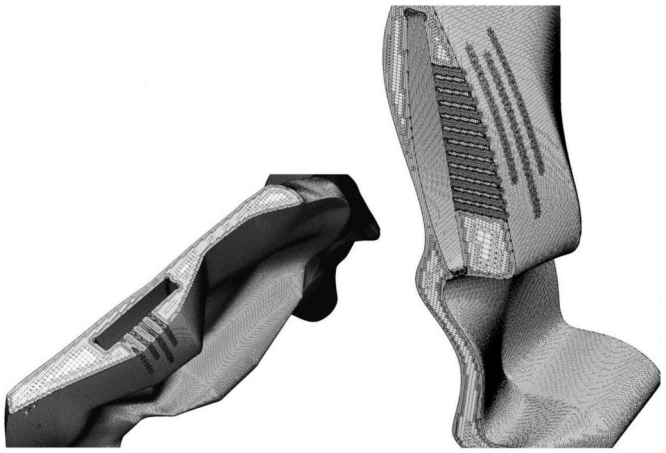

Fig. 9. Parts of the computational grid resulting from the SnappyHexMesh tool. The hollow space created by the obstacle shows the absence of fluid in that region. The left panel shows a *xy*-plane clip and the right panel a *xz*-plane clip. The rods are seen in the mesh. Note how the mesh is refined in these regions.

Table 1
Boundary conditions in the CFD calculations. Each italic term is a B.C. class in OpenFOAM. The *pressureInletOutletVelocity* condition is typically paired with the *totalPressure*. This is known to improve the stability of simulation by allowing the minor backflows at the outlet.

Boundary	Pressure	Velocity
Inlet	*zeroGradient* ($\frac{\partial p}{\partial n} = 0$)	*flowRateInletVelocity* ($Q = 15\ L/min$)
Outlet	*totalPressure* ($p_0 = 0$)	*pressureInletOutletVelocity*
Other regions	Same as Inlet boundary	*noSlip* ($\boldsymbol{u} = 0$)

cases. Within SIMPLE, each field is solved by a specific algorithm within the linear inner iterations. The velocity field was solved by the Gauss-Seidel method. The pressure field was solved by the Geometrically Algebraic Multigrid (GAMG) method, which is preconditioned by the Diagonally Incomplete Cholesky (DIC) method. GAMG is a quick method that begins with a coarse mesh. The level of detail in the mesh increases until the convergence in the pressure field is reached. Compared to DIC and diagonal pressure solvers, a faster converging solution was observed by using the DIC-preconditioned GAMG.

Spatial discretization was second order using Gauss linear with cell limiting. Grid convergence was studied to determine the number of cells required to achieve grid independence (within 10%) for the value of the pressure drop through the airway. The boundary conditions were the same as in the realistic simulations of [27] (see Table 1). Each of these conditions is defined according to boundary condition specifications provided by OpenFOAM. Special attention was paid to the boundary conditions to ensure the numerical stability of the SIMPLE iterations. The flow rate at the inlet was fixed at 15 l/min. This is the flow rate through a single nostril.

2.3. Lagrangian particle tracking

After solution of the velocity and pressure fields, particle tracking was performed. The particles were assumed to be non-evaporating and were assumed to stick to all boundary surfaces. Stuck and escaped particles were labelled by OpenFOAM and were no longer updated during the rest of the particle tracking iterations.

The momentum of the particles was assumed to be one-way coupled with that of the fluid, i.e. the particles do not disturb the flow. Particle position was updated using Newton's second law

$$m_p\left(\frac{du_p}{dt}\right)^i = F_D + F_b \tag{1}$$

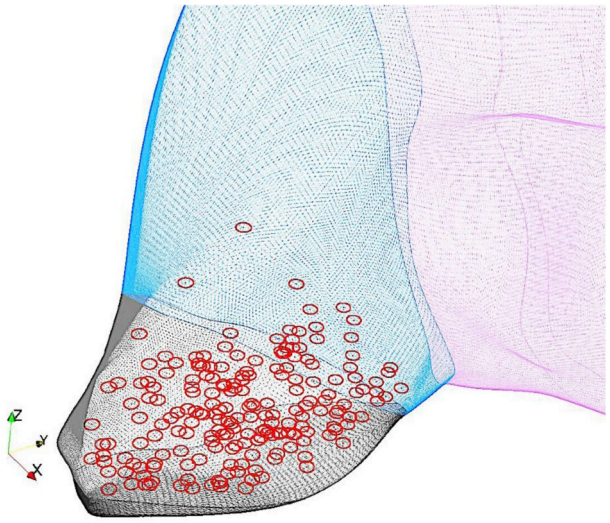

Fig. 10. Positions of particle injection at the entrance are shown. Circles show the location and alignment of the tip of the injector. Centers of circles were randomly chosen and were offset a minimum of 1mm from the walls. Particles were introduced randomly on the surface of each disk. The injection half-cone inner and outer angles were set at 0° (+ z direction) and 15°. The injection direction for an individual particle is interpolated between the inner and outer half cone angle based on the location at which it appears on the injection disk.

where F_D is the drag force and F_b is the force of gravity (including any buoyancy effects) at the i^{th} time-step on the p^{th} particle. In steady one-way coupling, F_D depends on the difference between the velocity field u_f, which remains constant at a given location, and the particle velocity u_p in the usual manner via a drag coefficient. Here, we employed the Schiller-Neumann formula for drag coefficient:

$$C_D = \frac{24}{Re_P}(1 + 0.17\ Re_P^{0.66}) \tag{2}$$

with the kinematic viscosity of the air set to $\nu = 1.5 \times 10^{-5}\frac{m^2}{s}$. The velocity of the fluid was interpolated to the location of the particle using the linear cell method. The implicit Euler method was used for time integration of particle trajectory. The implicit Euler method is known to be unconditionally stable; however, due to nonlinearity of the flow field, extra caution is exercised by performing time step size analysis. A convergence analysis of the number of injected particles was conducted to ensure that the number of particles (10,000) was satisfactory.

Lagrangian particle tracking was accomplished using the IcoUncoupledKinematicParcelFoam (IUKPF) application of Open FOAM. IUKPF was further customized by compiling a local code via OpenFOAM's WMake utility. IUKPF utilizes a simplified version of the general Kinematic Cloud (KC) objects for particles and assumes them to be uncoupled with respect to each other. The main OpenFOAM required dictionary file name is KC-Properties and contains necessary values used by IUKPF. Since IUKPF is a very simplified particle tracking method, most entries of KC-Properties were not set.

To explore the possibility of different injection positions and their impact on the deposition results, the tip of the particle spray injection was placed at various locations specified randomly within the entrance region. The deposition results were then averaged among all these random locations. In order to generate random locations for the tip of the injector, a VTK location generator code was used. Particles were injected within the nostril from a planar disk region with 1 mm diameter; the position of the disk was varied within the nares to define 200 random positions. The injection location was varied from just inside the entrance of the nares to just after the entrance of the nasal valve region, with these insertion depths varying approximately in the range of 0.1–1.5 cm from the inlet. Fig. 10 shows the randomly generated

Table 2
Particle parameters. These are used in idealized geometry particle tracking simulations. For the validation case the number of particle tracking cases is 4000.

Parameter	Number of Variants	Values
Particle diameter	5	{5, 10, 15, 20, 40} microns
Injection cone angle	2	0° inner and 15° outer
Injection direction	1	Upward (+ z)
Particle injection velocity	4	{0, 5, 10, 20} m/s
Position of center point of injection disk (Only for the final validation case)	200	Randomly located within entrance and 1 mm offset from walls. 10,000 particles released randomly on surface of each disk location.

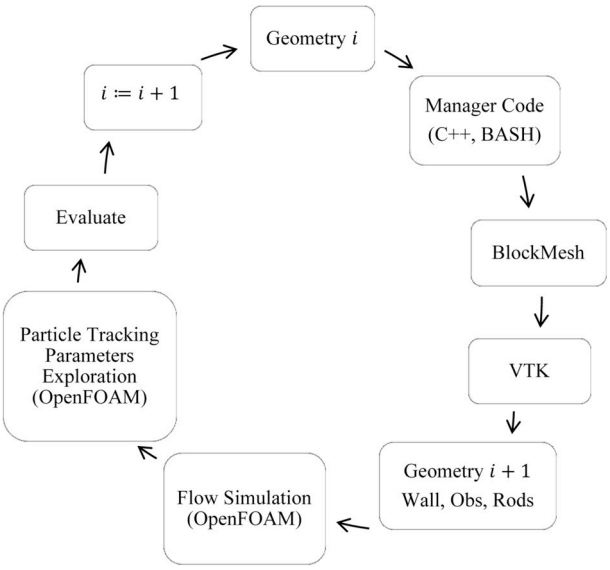

Fig. 11. The complete iterative procedure used in the development of the idealized airway.

injection disks within the nares.

Particle injection occurred at a constant velocity. Because of the one-way coupled assumption, the injection volumetric flow rate is arbitrary. Ten thousand particles were injected through each disk, with average particle initial velocity in the +z direction but distributed to form a cone shape injector with specified inner and outer angles of 0 and 15°. These parameters were chosen from a subset of the ones used for the realistic geometry simulations and they were based on that seen in typical nasal spray devices.

Table 2 shows the combination of parameters used for particle tracking simulations in this study. Because of the iterative process used in designing the idealized geometry, the number of injection positions was kept low during iteration of the geometry shape; a total of 80 particle tracking simulations per idealized geometry parametrization were performed at this stage. However, for the final idealized geometry, 4000 simulations were performed. The latter is consistent with the parameter set used in the realistic geometry study of [27].

Several Bourne Again Shell (Bash) scripts were developed to detect idle CPU threads for use in simultaneous particle tracking simulations. The simulations were done in parallel on a local Beowulf cluster which is based on the Network File System (NFS) (Sun Microsystem, USA) protocol. This cluster contains 20 threads overclocked at 4.2 GHz, 24 threads 2.4 GHz and 4 threads at 3.5 GHz, for a total of 48 threads. Memory in use was 200 GB. To calculate the regional deposition, the geometry was divided into the regions of vestibule, valve, turbinates, olfactory, nasopharynx and outlet. Additionally, the turbinates were subdivided into main wall, rods and obstacle. The diagram of the full iterative process is shown in Fig. 11.

2.4. Evaluation of the quality of an idealized geometry

In this study the development of the idealized geometry was based on a few iterations that involved starting with an initial idealized geometry and iteratively distorting this geometry with the aim of achieving a closer and closer match to average deposition seen in the different regions of the realistic geometries. In order to evaluate each

Fig. 12. Monolithic Idealized Geometry: The Y-shaped cross sections of the idealized geometry are shown on the left. The surface of the geometry is shown on the right. This specific geometry is called a monolithic surface because (1) the geometry is made solely with sequences of blocks in BlockMesh and (2) the cross sections remain homeomorphic with respect to each other. The cross sections in colors show the simply-connected behaviour of curves in the turbinate region of this geometry.

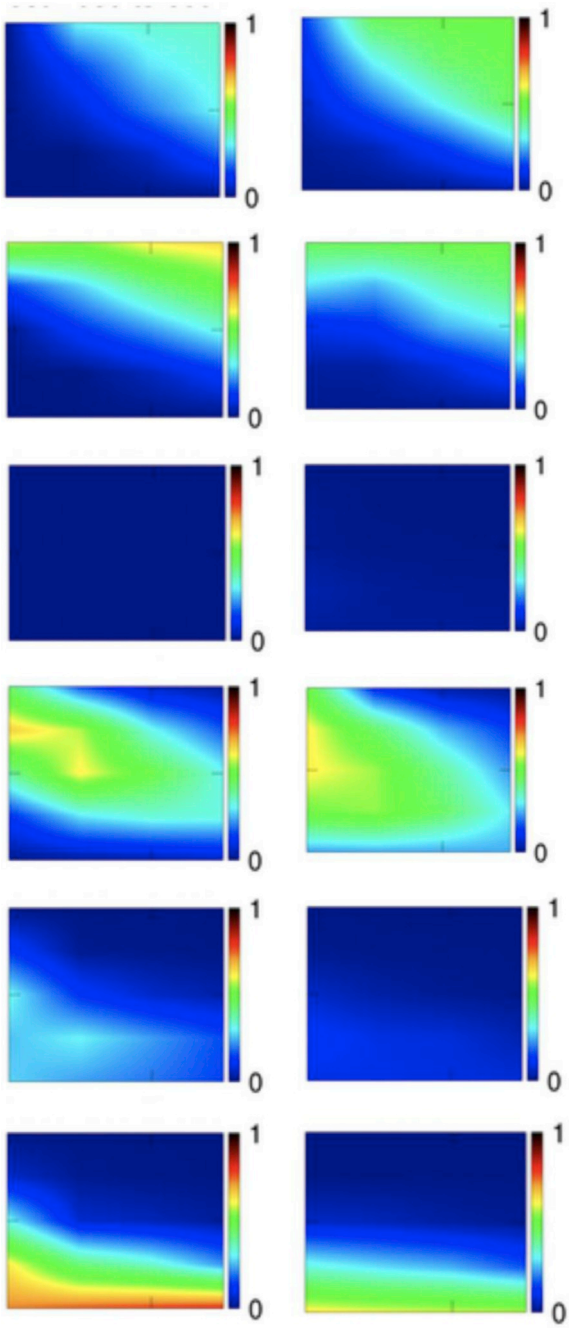

Fig. 13. Monolithic Idealized Geometry: Each row denotes a certain region (in order: Vestibule, Valve, Olfactory, Turbinates, Nasopharynx, Outlet). The deposition fraction in the monolithic idealized geometry (plots in left column) and averaged over the realistic geometries (plots in right column) are shown. The vertical axis in each plot denotes the particle diameter (5–40 μm) while the horizontal axes are the particle initial velocities (0–20 m/s). Note that small particles are not well captured at lower spray velocities by the turbinate region of the idealized geometry in this case. The color scale is interpolated and shows the deposition fraction (0–1) out of total particles.

geometry modification, a norm was needed. For this purpose, let C be a functional associated with the CFD results and L a functional associated with the Lagrangian particle tracking fields, while M is the functional representing a regional average deposition matrix, with its rows based on particle diameters and its columns based on particle initial velocity:

$$\mathbf{M}(\mathbf{x}) = \mathbf{L}(\mathbf{C}(\mathbf{S}(\mathbf{x}))) \tag{3}$$

With this formalism, an objective function can be defined as

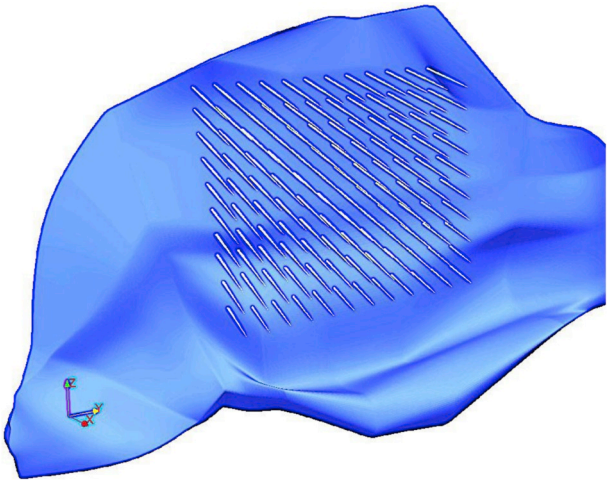

Fig. 14. Idealized Geometry with Rods: A penultimate version of the idealized geometry is shown. A grid of rods (shown in the brighter color) is penetrates the turbinate region side. The rods protrude in the x-direction across the full breadth of the turbinates airway.

$f(x) = |M(x) - M_{ref}|$ in which $|\ .\ |$ denotes a norm, and the optimization problem in design space Γ devolves to finding S:

$$\arg \min_{\mathbf{x}\in\Gamma} \mathbf{f}(\mathbf{S}) \tag{4}$$

The latter equation describes a multi-objective optimization problem; i.e. there is no unified solution capable of minimizing all components of **f** simultaneously. Using the weighted scalarizing method, the objective function can be represented as

$$\mathbf{f}(\boldsymbol{x}) = \sum_{j} w^{j} \sqrt{\sum_{u=1}^{4}\sum_{d=1}^{5}\left(m^{j}_{du}(\mathbf{x}) - m^{j}_{duref}\right)^{2}} \tag{5}$$

in which m^j are the components of the deposition matrix M^j. The indices d, u and j denote particle diameters, initial velocities and nose regions respectively. The subscript *ref* denotes average deposition in the corresponding realistic geometries. Eqn. (5) can be thought of as a generalized least squares minimization problem in which the shape of the geometry is adjusted to minimize the given sum of squares.

By assuming $w^j = 1$, the previous expression becomes the sum of L^2 norms of the regional deposition. This value of the norm was used to provide a measure for evaluating whether or not a given realization of the idealized geometry was close to giving the target values of average deposition in the realistic geometries. Despite repeated efforts by us to use automated iterative optimization algorithms to deform a starting idealized geometry into a finalized idealized geometry that minimized the objective function, such an approach was finally abandoned due to the myriad number of stationary points in the resulting high-dimensional space. Instead, an heuristic approach to achieving the finalized idealized geometry was followed.

3. Results and discussion

3.1. Monolithic idealized geometry

The main wall of the surface geometry was constructed by arranging skeleton splines. The number of possible geometries is infinite. The cross sections are homeomorphic in this case. A slight modification in a control point of a spline results in a smooth change of the surface geometry. Through iterations over the control points of the main wall, many geometry versions are created. Fig. 12 shows one of these geometries that provides reasonable regional deposition values. Fig. 13 shows the regional deposition results. Although the overall behaviour is good, the small particles are not captured in the turbinates.

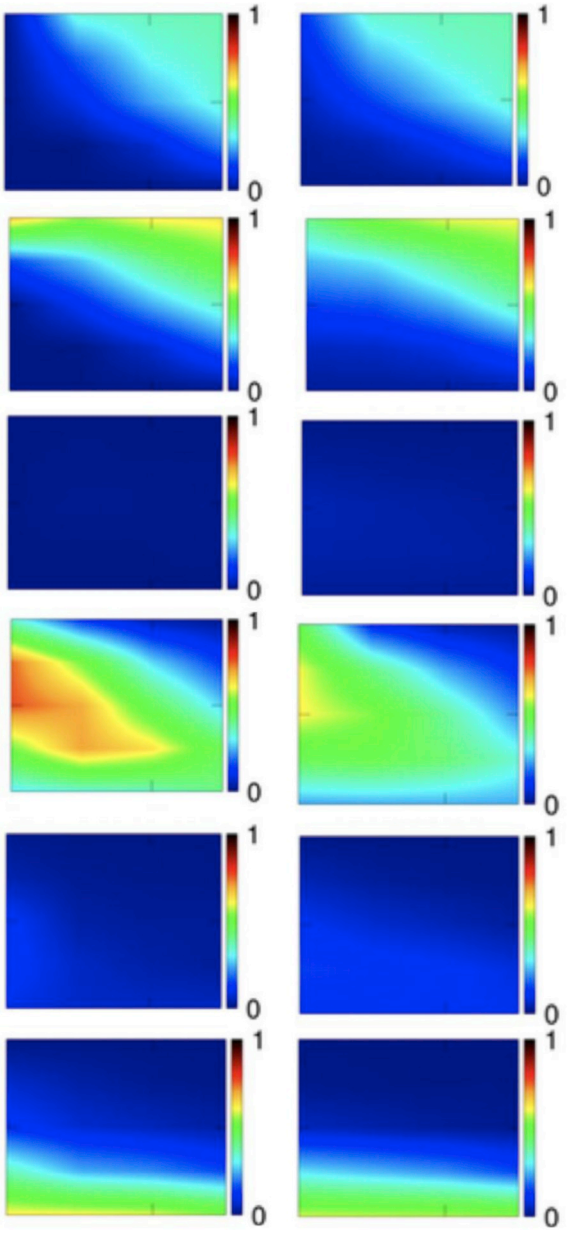

Fig. 15. Idealized Geometry with Rods: Each row denotes a certain region (in order: Vestibule, Valve, Olfactory, Turbinates, Nasopharynx, Outlet). The deposition fraction in the idealized geometry with rods (plots in left column) and averaged over realistic geometries (plots in right column) are shown. The vertical axis in each plot denotes the particle diameter (5–40 μm) while the horizontal axes are the particle initial velocities (0–20 m/s). Note that particle deposition is too great in the turbinates in this case. The color scale is interpolated and shows the deposition fraction (0–1) out of total particles.

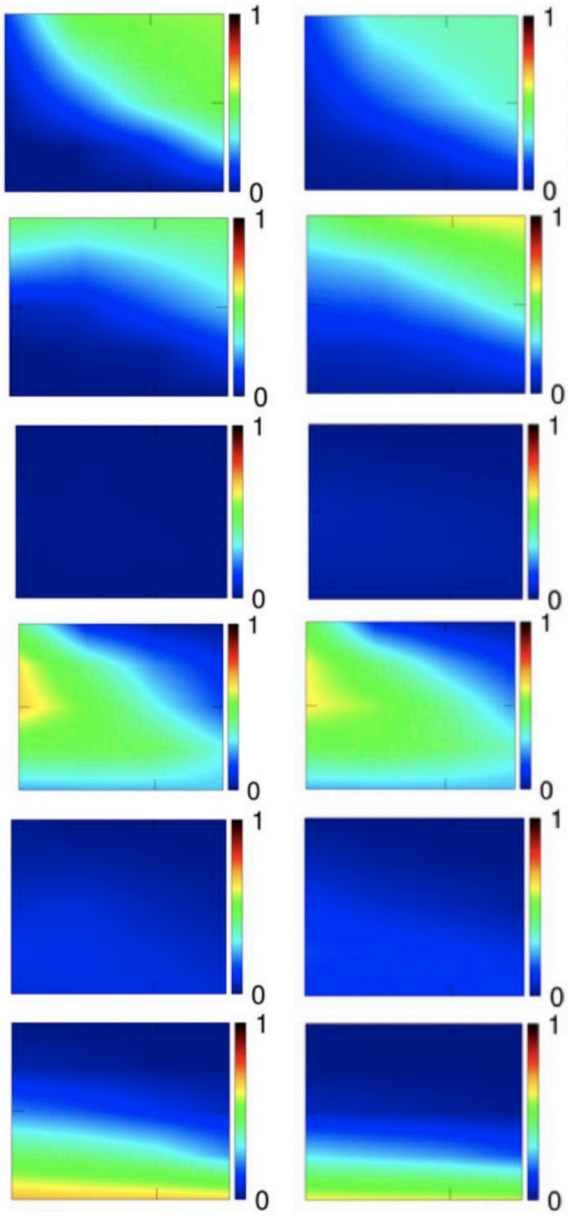

Fig. 16. Idealized Geometry with Obstacle and Rods: Each row denotes a certain region (in order: Vestibule, Valve, Olfactory, Turbinates, Nasopharynx, Outlet). The deposition fraction in the virtual impactor idealized geometry (plots in left column) and averaged over realistic geometries (plots in right column) are shown. The vertical axis in each plot denotes the particle diameter (5–40 μm) while the horizontal axes are the particle initial velocities (0–20 m/s). The color scale is interpolated and shows the deposition fraction (0–1) out of total particles.

Consequently, the nasopharynx and outlet experience more particle deposition and escape, respectively. This behaviour contradicts the average behaviour in the realistic geometries which is shown in the right column of Fig. 13.

3.2. Idealized geometry with rods

With the intention of capturing more of the small particles, rods were introduced in the turbinates of the geometry. After careful evaluation of different sizes of rods, a diameter of 0.2 mm was chosen. Fig. 14 shows a grid of rods distributed over the idealized geometry aligned on the x axis. As shown in Fig. 15, turbinate deposition improved for the small particles. However, too many mid-sized particles were deposited in the turbinates. This suggests that adding a mechanism capable of separating the particles by size could be used to improve the regional deposition results.

3.3. Idealized geometry with Obstacle and Rods

Two impactor type deposition mechanisms were inspired by observations of the realistic geometries. In particular, the previously noted obstacle feature (Fig. 7) had a trivial equivalence in the complex realistic geometries, and small-scale geometric traps for the smaller particles were mimicked using small rods in the idealized geometry. Adding the obstacle in the middle of the turbinate region created two

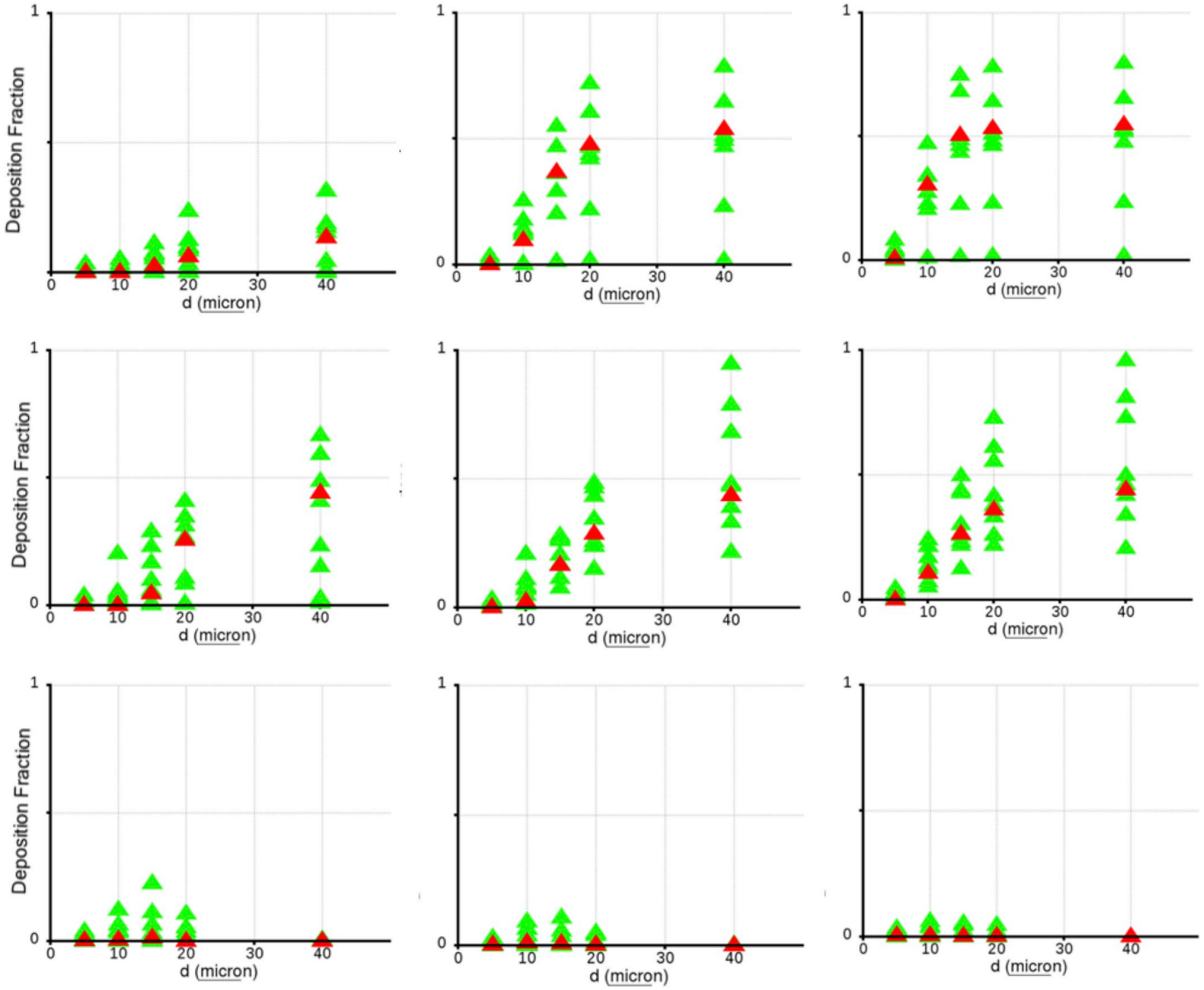

Fig. 17. Idealized Geometry with Obstacle and Rods: Each triple plot in a row denotes a certain region (in order: Vestibule, Valve, Olfactory, Turbinates, Nasopharynx, Outlet). Each column shows an initial particle velocity (from left to right 0, 10 and 20 m/s). The green marker shows average regional deposition in different individual realistic subjects (from Ref. [27] while the red marker shows the regional deposition in the final idealized geometry. The vertical axis is the fraction (0–1) of 10000 particles.

paths, similar to a virtual impactor, while adding the rods to the major flow branch further improved the regional deposition. Fig. 16 shows the regional deposition results for this case. Since the results were a very good match, the same 200 random injection positions at the entrance used previously in the realistic geometries were then applied to this final idealized geometry. As a result, the deposition matrices smoothed further and resulted in nearly identical turbinate deposition. Fig. 17 shows the deposition values in the final idealized geometry versus all seven realistic geometries studied by Ref. [27]. The deposition in the idealized geometry is typically in the middle of the range of those in the realistic geometries.

3.4. Further discussion

As discussed in the introduction, when developing devices and formulations for intranasal drug delivery, it is typically desirable to target deposition to the turbinate regions. For the final idealized geometry, the largest deposition in the turbinate regions occurs for intermediate particle sizes. This result is in agreement with CFD simulations in Ref. [27] as well as with the majority of cases studied by others [15]. Turbinate deposition is also largest for zero spray velocity. In combination, these results are explained by the fact that if the particle is too large, or its velocity is too high, it will impact the entrance wall due to high inertia. In the opposite case, small particles will penetrate the nasal geometry and escape through the outlet. Hence the zero-velocity intermediate sized particles are the ones most likely to deposit in the turbinate region. The average olfactory deposition was nearly zero, as expected. This result is consistent with previous studies [27,31,32]. Penetration remained mostly as observed in the average realistic geometries.

Two main impaction mechanisms were necessary to mimic deposition in the turbinate region. The conventional impaction is the main mechanism responsible for the medium and large particle deposition occurring at the front face and -x side of the obstacle. However, a virtual impactor mechanism functions at the +x the side of the obstacle. A fraction of the remaining small particles that escaped the obstacle were deposited on the rods on this side. The 0.2 mm diameter chosen for the rods was near the optimum value for collecting the small particles. Larger diameters (e.g. 1 mm) tended to disturb the flow, causing particles to follow a path around the larger rods. On the other hand,

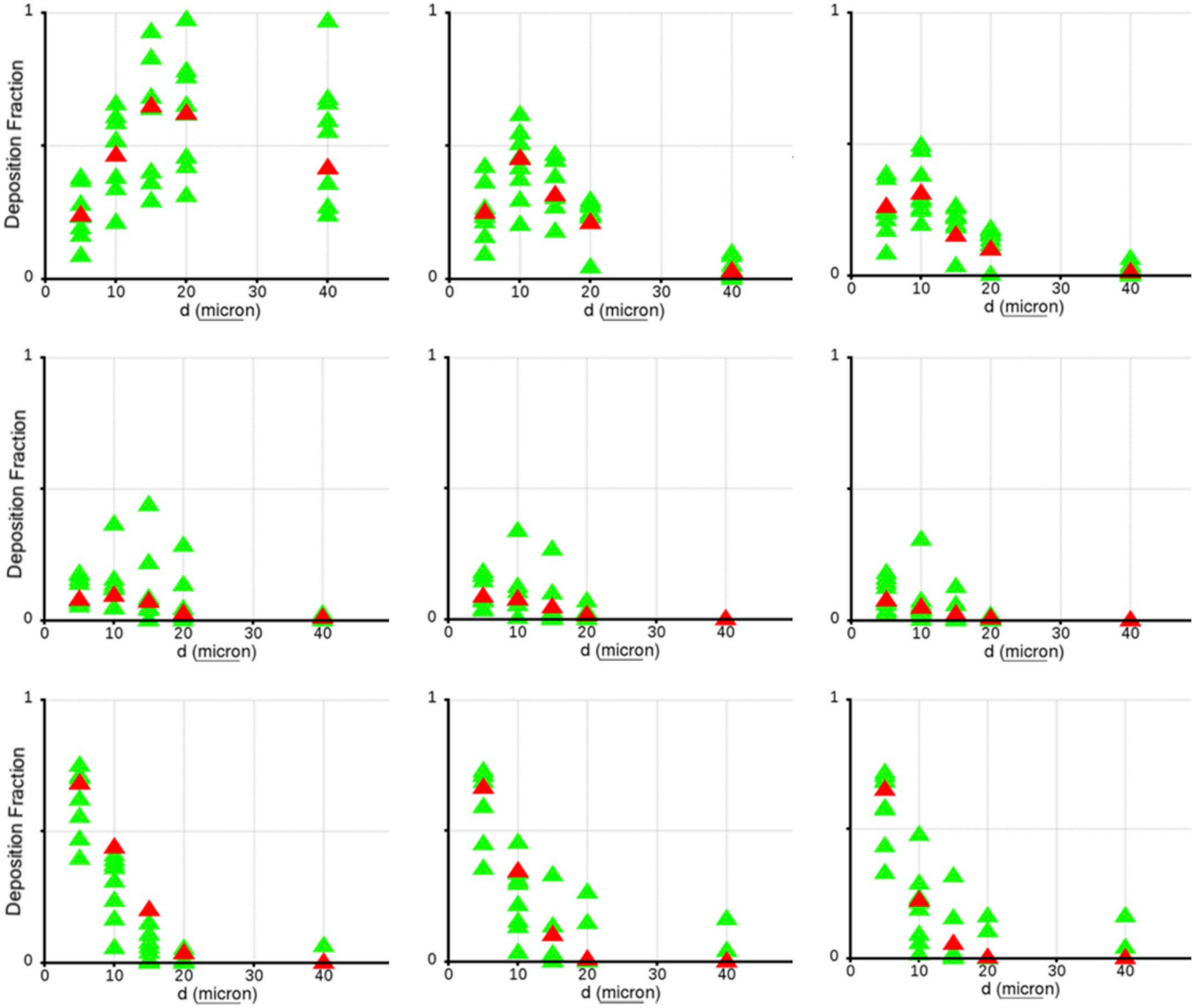

Fig. 17. (*continued*)

smaller rod diameters would make manufacturing more difficult. Furthermore, the rods' angle of inclination plays an effective role in collecting more of small particles. The angles achieve this goal by reducing the rods' overlap.

It should be noted that our use of regional deposition data simulated in normal (non-pathological) nasal airway geometries as a target for evaluating the proposed idealized geometry may limit the ability of the idealized geometry to mimic regional deposition that occurs in patients with pathological nasal airways. Though direct comparison of regional deposition patterns in normal versus pathological nasal airways is scarce, Weber at al [33]. reported a slightly higher fraction of budesonide nasal spray depositing in the turbinates region of patients with previous paranasal sinus surgery compared with that in healthy subjects without previous nasal surgery. It is a reasonable hypothesis that for a patient with a nasal condition, or history of nasal surgery, which significantly alters the nasal airway geometry, deposition patterns may differ from those predicted using an idealized geometry that mimics deposition in normal nasal airways. This potential limitation of the idealized geometry proposed herein is more likely to present an issue for testing nasal sprays or delivery devices intended for topical treatment, as opposed to those intended for systemic drug administration. In the latter case, patients using medications delivered intranasally for, e.g., relief from migraine headaches, treatment of breakthrough pain, or opioid overdose, will predominantly have normal nasal airways.

An additional limitation of the present study is in the use of an heuristic approach to achieve the proposed idealized geometry. Although use of automated iterative optimization algorithms was explored, ultimately use of these algorithms proved unsuccessful. As such, whether or not some different geometry is capable of emulating average regional deposition patterns more closely than the idealized geometry proposed here remains unproven. That said, Fig. 17 provides evidence that regional deposition simulated in the present idealized geometry typically falls in the middle of the data range for realistic geometries studied by Ref. [27]. This provides motivation to carry the proposed idealized geometry forward for further evaluation in the form of in vitro testing of nasal spray formulations.

4. Conclusion

The aim of this study was to use computational methods to develop an idealized nasal airway geometry capable of mimicking the regional deposition pattern observed in a set of realistic geometries. Regional deposition in the idealized geometry was found to be in good agreement with the median of that seen for regional deposition in the realistic

geometries. The present idealized geometry may be a useful benchtop tool for in vitro research and development of nasal spray formulations. The idealized geometry also has the potential to be used as a reference geometry in modelling and simulations performed to investigate pharmaceutical nasal sprays and other intranasal drug delivery devices.

Conflict of interest

No conflict of interest exist.

Acknowledgment

WHF and ARM gratefully acknowledge funding from the Natural Sciences and Engineering Research Council of Canada.

References

[1] C.L. Leach, P.J. Kuehl, R. Chand, J.D. McDonald, Nasal deposition of HFA-beclomethasone, aqueous fluticasone propionate and aqueous mometasone furoate in allergic rhinitis patients, J. Aerosol Med. Pulm. Drug Deliv. 28 (5) (2015) 334–340.
[2] P.G. Djupesland, A. Skretting, Nasal deposition and clearance in man: comparison of a bidirectional powder device and a traditional liquid spray pump, J. Aerosol Med. Pulm. Drug Deliv. 25 (5) (2012) 280–289.
[3] P.G. Djupesland, A. Skretting, M. Winderen, T. Holand, Bi-directional nasal delivery of aerosols can prevent lung deposition, J. Aerosol Med. 17 (3) (2004) 249–259.
[4] J.D. Suman, B.L. Laube, R. Dalby, Comparison of nasal deposition and clearance of aerosol generated by a nebulizer and an aqueous spray pump, Pharm. Res. (N. Y.) 16 (10) (1999) 1648–1652.
[5] S.E. Churchill, L.L. Shackelford, J.N. Georgi, M.T. Black, Morphological variation and airflow dynamics in the human nose, Am. J. Hum. Biol. 16 (6) (2004) 625–638.
[6] G.J.M. Garcia, E.W. Tewksbury, B.A. Wong, J.S. Kimbell, Interindividual variability in nasal filtration as a function of nasal cavity geometry, J. Aerosol Med. Pulm. Drug Deliv. 22 (2) (2009) 139–156.
[7] P.R. Byron, M. Hindle, C.F. Lange, P.W. Longest, D. McRobbie, M.J. Oldham, B. Olsson, C.G. Thiel, H. Wachtel, W.H. Finlay, *In vivo–in vitro* correlations: predicting pulmonary drug deposition from pharmaceutical aerosols, J. Aerosol Med. Pulm. Drug Deliv. 23 (S2) (2010) S-59-S-69.
[8] I. Hahn, P.W. Scherer, M.M. Mozell, Velocity profiles measured for airflow through a large-scale model of the human nasal cavity, J. Appl. Physiol. 75 (1993) 2273–2287.
[9] J. Heyder, Deposition of inhaled particles in the human respiratory tract and consequences for regional targeting in respiratory drug delivery, Proc. Am. Thorac. Soc. 1 (4) (2004) 315–320.
[10] J. Heyder, G. Rudolf, Deposition of aerosol particles in the human nose, Inhaled Part. 4 (Pt 1) (1975) 107–126.
[11] E. Javaheri, L. Golshahi, W.H. Finlay, An idealized geometry that mimics average infant nasal airway deposition, J. Aerosol Sci. 55 (2013) 137–148.
[12] Y. Liu, E.A. Matida, M.R. Johnson, Experimental measurements and computational modeling of aerosol deposition in the Carleton-Civic standardized human nasal cavity, J. Aerosol Sci. 41 (6) (2010) 569–586.
[13] J.D. Schroeter, E.W. Tewksbury, B.A. Wong, J.S. Kimbell, Experimental measurements and computational predictions of regional particle deposition in a sectional nasal model, J. Aerosol Med. Pulm. Drug Deliv. 28 (1) (2015) 20–29.
[14] S. a Shah, C.J. Dickens, D.J. Ward, A. a Banaszek, C. George, W. Horodnik, Design of experiments to optimize an in vitro cast to predict human nasal drug deposition, J. Aerosol Med. Pulm. Drug Deliv. 26 (1) (2013) 1–9.
[15] J.A. Keeler, A. Patki, C.R. Woodard, D.O. Frank-Ito, A computational study of nasal spray deposition pattern in four ethnic groups, J. Aerosol Med. Pulm. Drug Deliv. 28 (0) (2015) 1–14.
[16] R.G. Patel, G.J.M. Garcia, D.O. Frank-Ito, J.S. Kimbell, J.S. Rhee, Simulating the nasal cycle with computational fluid dynamics, Otolaryngol. Head Neck Surg. 152 (2) (2015) 353–360.
[17] J.S. Rhee, S.S. Pawar, G.J.M. Garcia, J.S. Kimbell, Toward personalized nasal surgery using computational fluid dynamics, Arch. Facial Plast. Surg. 13 (5) (2011) 305.
[18] J.D. Schroeter, G.J.M. Garcia, J.S. Kimbell, A computational fluid dynamics approach to assess interhuman variability in hydrogen sulfide nasal dosimetry, Inhal. Toxicol. 22 (4) (2010) 277–286.
[19] J.D. Schroeter, J.S. Kimbell, B. Asgharian, E.W. Tewksbury, M. Singal, Computational fluid dynamics simulations of submicrometer and micrometer particle deposition in the nasal passages of a Sprague-Dawley rat, J. Aerosol Sci. 43 (1) (2012) 31–44.
[20] D.Y. Wang, H.P. Lee, B.R. Gordon, Impacts of fluid dynamics simulation in study of nasal airflow physiology and pathophysiology in realistic human three-dimensional nose models, Clin. Exp. Otorhinolaryngol. 5 (4) (2012) 181–187.
[21] I. Weinhold, G. Mlynski, Numerical simulation of airflow in the human nose, Eur. Arch. Oto-Rhino-Laryngol. 261 (8) (2004) 452–455.
[22] A. Below, D. Bickmann, J. Breitkreutz, Assessing the performance of two dry powder inhalers in preschool children using an idealized pediatric upper airway model, Int. J. Pharm. 444 (1–2) (2013) 169–174.
[23] R.R. Delvadia, P.W. Longest, P.R. Byron, *In vitro* tests for aerosol deposition. I: scaling a physical model of the upper airways to predict drug deposition variation in normal humans, J. Aerosol Med. Pulm. Drug Deliv. 25 (1) (2012) 32–40.
[24] L. Golshahi, W.H. Finlay, An idealized child throat that mimics average pediatric oropharyngeal deposition, Aerosol Sci. Technol. 46 (5) (2012) i–iv.
[25] S. Tavernini, T.K. Church, D.A. Lewis, A.R. Martin, W.H. Finlay, Scaling an idealized infant nasal airway geometry to mimic inertial filtration of neonatal nasal airways, J. Aerosol Sci. 118 (2018) 14–21.
[26] Y. Liu, M.R. Johnson, E.A. Matida, S. Kherani, J. Marsan, Creation of a standardized geometry of the human nasal cavity, J. Appl. Physiol. 106 (3) (2009) 784–795.
[27] M. Kiaee, H. Wachtel, M.L. Noga, A.R. Martin, W.H. Finlay, Regional deposition of nasal sprays in adults: a wide ranging computational study, Int. J. Numer. Method. Biomed. Eng. 34 (5) (2018) e2968.
[28] N. Kawara, M. Kumita, H. Kurachi, T. Seto, S. Kamba, T. Kondo, Y. Otani, Sieving of aerosol particles with metal screens, Aerosol Sci. Technol. 50 (6) (2016) 535–541.
[29] K. Keyhani, P.W. Scherer, M.M. Mozell, Numerical simulation of airflow in the human nasal cavity, J. Biomech. Eng. 117 (4) (1995) 429.
[30] S. Schreck, K.J. Sullivan, C.M. Ho, H.K. Chang, Correlations between flow resistance and geometry in a model of the human nose, J. Appl. Physiol. 75 (4) (1993) 1767–1775.
[31] J.D. Schroeter, J.S. Kimbell, B. Asgharian, Analysis of particle deposition in the turbinate and olfactory regions using a human nasal computational fluid dynamics model, J. Aerosol Med. 19 (3) (2006) 301–313.
[32] J. Xi, J.E. Yuan, Y. Zhang, D. Nevorski, Z. Wang, Y. Zhou, Visualization and quantification of nasal and olfactory deposition in a sectional adult nasal airway cast, Pharm. Res. (N. Y.) 33 (6) (2016) 1527–1541.
[33] R. Weber, R. Keerl, R. Radziwill, B. Schick, D. Jaspersen, K. Dshambazov, G. Mlynski, W. Draf, Videoendoscopic analysis of nasal steroid distribution, Rhinology 37 (1999) 69–73.